Weighted-RXD and Linear Filter-Based RXD: Improving Background Statistics Estimation for Anomaly Detection in Hyperspectral Imagery

Qiandong Guo, Bing Zhang, *Senior Member*, *IEEE*, Qiong Ran, Lianru Gao, *Member*, *IEEE*, Jun Li, and Antonio Plaza, *Senior Member*, *IEEE*

Abstract—Anomaly detection is an active topic in hyperspectral imaging, with many practical applications. Reed-Xiaoli detector (RXD), a widely used method for anomaly detection, uses the covariance matrix and mean vector to represent background signals, assuming that the background information adjusts to a multivariate normal distribution. However, in general, real images present very complex backgrounds. As a result, in many situations, the background information cannot be properly modeled. An important reason is that that background samples often contain also anomalous pixels and noise, which lead to a high false alarm rate. Therefore, the characterization of the background is essential for successful anomaly detection. In this paper, we develop two novel approaches: weighted-RXD (W-RXD) and linear filter-based RXD (LF-RXD) aimed at improving background in RXD-based anomaly detection. By reducing the weight of the anomalous pixels or noise signals and increasing the weight of the background samples, W-RXD can provide better estimations of the background information. In turn, LF-RXD uses the probability of each pixel as background to filter wrong anomalous or noisy instances. Our experimental results, intended to analyze the performance of the newly developed anomaly detectors, indicate that the proposed approaches achieve good performance when compared with other classic approaches for anomaly detection in the literature.

Index Terms—Anomaly detection, covariance matrix estimation, hyperspectral imagery, linear filter (LF), linear filter-based RXD (LF-RXD), RXD, weighted-RXD (W-RXD).

Q. D. Guo, B. Zhang, and L. R. Gao are with the Key Laboratory of Digital Earth Science, Institute of Remote Sensing and Digital Earth, Chinese Academy of Sciences, Beijing 100094, China (e-mail: zb@radi.ac.cn; gaolr@radi.ac.cn).

Q. D. Guo is with the University of Chinese Academy of Sciences, Beijing 100049, China (e-mail: guoqd@radi.ac.cn).

Q. Ran is with the College of Information Science and Technology, Beijing University of Chemical Technology, Beijing 100029, China (e-mail: qiong_ran@163.com).

J. Li is with the School of Geography and Planning, Sun Yat-Sen University, Guangzhou 510275, China (e-mail: jun@lx.it.pt).

A. Plaza is with the Department of Technology of Computers and Communications, Escuela Politécnica, University of Extremadura, 10003 Cáceres, Spain (e-mail: aplaza@unex.es).

Color versions of one or more of the figures in this paper are available online at http://ieeexplore.ieee.org.

I. INTRODUCTION

TARGET and anomaly detection play a significant role in hyperspectral imaging applications. Unlike conventional detection methods, which obtain information from high spatial resolution images, hyperspectral imaging allows uncovering targets from the background by taking advantage of the very fine spectral resolution provided by this kind of data. Based on the availability of *a priori* target information, we can roughly categorize hyperspectral target detection methods into three main classes: 1) anomaly detection without any prior information (e.g., known target spectra [1], [2]); 2) signature matching-based detection for problems in which the target is defined by a single reference spectrum [3], [4]; and 3) subspace-matched detection for problems in which a target is represented by a set of basis vectors which account for target signal variation [5], [6]. In this work, we specifically focus on the problem of anomaly detection.

Anomalies are targets or features of interest that have two main characteristics [1]. First and foremost, their spectral signatures are different to those associated to local background pixels. Furthermore, anomalous targets occur with low probabilities. Since anomaly detection has many practical applications, various algorithms have been developed for this purpose. One of the most widely used methods is the Reed-Xiaoli detector (RXD) [7]. This method assumes that the background follows a multivariate normal distribution. Based on this assumption, RXD uses the probability density function of a multivariate normal distribution in order to measure the probability of a pixel under test (PUT) to be part of the background. In many scenarios, however, this assumption does not hold. One reason is that the local background may be too complicated to be described by a multivariate normal distribution. Besides, RXD may not be efficient for removing anomalous signatures when estimating background information using the covariance matrix and the mean vector as a form of background representation. Hence, the background information may be contaminated by other anomalous and noisy signals. This causes the fact that some noise pixels or background pixels may be wrongly detected as anomalies. Other anomaly detection algorithms such as the random-selection-based anomaly detector (RSAD) and the blocked adaptive computationally efficient outlier nominator (BACON) method can prevent the contamination of anomalous signatures [8], [9] by removing anomalous signatures when estimating background information.

In this paper, we address this issue and further develop two variants of RXD, called weighted-RXD (W-RXD) and linear filter-based RXD (LF-RXD), intended to provide a more accurate estimation of the covariance matrix and mean vector of the background. The main goal of these methods is to remove the anomalous and noisy signals from the background information. Specifically, W-RXD assigns low weights to the samples with high probability to be declared as anomalies, and high weights to the samples with high probability to be declared as part of the background. Resulting from this process, we obtain a better balance between the anomalies and background signals. On the other hand, LF-RXD performs filtering of anomalies and noise in order to refine the estimation of the covariance matrix of the background, thus providing a more realistic characterization of the anomalies.

The remainder of paper is organized as follows. Section II presents an overview of the classic RXD algorithm and some of its variations. Section III introduces the newly developed methods for improving background statistics estimation. Section IV conducts a detailed evaluation of the discussed methods using synthetic data. Section V performs experiments using real hyperspectral data sets. Section VI draws some conclusions and provides hints at plausible future research lines.

II. THE RXD ALGORITHM AND ITS VARIATIONS

RXD is one of the most popular methods for hyperspectral anomaly detection. Let H_1 be the target signal and H_0 be the background signal. We intend to solve the following detection problem:

$$H_0 : \mathbf{x} = \mathbf{b} \tag{1}$$
$$H_1 : \mathbf{x} = \mathbf{s} + \mathbf{b} \tag{2}$$

where $\mathbf{x}$ is a sample pixel vector, $\mathbf{s}$ is the target signal, and $\mathbf{b}$ is the background clutter, which follows a normal distribution with mean vector $\boldsymbol{\mu}$, and covariance matrix $\boldsymbol{\Sigma}$, i.e., $\mathbf{b} \sim N(\boldsymbol{\mu}, \boldsymbol{\Sigma})$. Therefore, we have $\mathbf{x}|H_0 \sim N(\boldsymbol{\mu}, \boldsymbol{\Sigma})$ and $\mathbf{x}|H_1 \sim N(\boldsymbol{\mu} + \mathbf{s}, \boldsymbol{\Sigma})$. With these definitions in mind, we obtain

$$p(\mathbf{x}|H_0) = \frac{1}{(2\pi)^{K/2}|\boldsymbol{\Sigma}|^{1/2}} e^{-\frac{1}{2}(\mathbf{x}-\boldsymbol{\mu})^T \boldsymbol{\Sigma}^{-1}(\mathbf{x}-\boldsymbol{\mu})} \tag{3}$$

where K is the number of bands in the original hyperspectral image. Since an anomalous pixel $\mathbf{x}_s$ is expected to be significantly different from the background, $p(\mathbf{x}_s|H_0)$ should be very small for an anomalous pixel. Therefore, for a certain background set, as $\frac{1}{(2\pi)^{K/2}|\boldsymbol{\Sigma}|^{1/2}}$ is fixed, $(\mathbf{x}_s - \boldsymbol{\mu})^T \boldsymbol{\Sigma}^{-1}(\mathbf{x}_s - \boldsymbol{\mu})$ should be larger for an anomalous pixel than for a background pixel. Based on this observation, RXD identifies anomalies using the following expression:

$$D_{RXD}(\mathbf{x}) = (\mathbf{x} - \boldsymbol{\mu})^T \boldsymbol{\Sigma}^{-1}(\mathbf{x} - \boldsymbol{\mu}). \tag{4}$$

There are several ways to obtain background samples for estimating $\boldsymbol{\Sigma}$ and $\boldsymbol{\mu}$. The global RXD (GRXD) and the local RXD (LRXD) use different strategies. Specifically, GRXD uses the following expression:

$$D_{GRXD}(\mathbf{x}) = (\mathbf{x} - \boldsymbol{\mu}_G)^T \boldsymbol{\Sigma}_G^{-1}(\mathbf{x} - \boldsymbol{\mu}_G) \tag{5}$$

where $\boldsymbol{\mu}_G$ and $\boldsymbol{\Sigma}_G$ are the mean vector and the covariance matrix of all pixels in the image. The LRXD, in turn, uses a local neighborhood around the PUT in order to perform the detection. Let us assume that $\boldsymbol{\mu}_8$ denotes the mean value of the eight-pixel neighborhood around the PUT. In this case, the LRXD performs the detection using the following expression:

$$D_{LRXD}(\mathbf{x}) = (\mathbf{x} - \boldsymbol{\mu}_8)^T \boldsymbol{\Sigma}_G^{-1}(\mathbf{x} - \boldsymbol{\mu}_8). \tag{6}$$

Here, it should be noted that LRXD generally uses $\boldsymbol{\Sigma}_G$ as the covariance matrix instead of $\boldsymbol{\Sigma}_8$. This is because in hyperspectral data, the number of spectral bands is higher than 8 and, in this case, $\boldsymbol{\Sigma}_8$ is a singular matrix and cannot be inverted [10].

The RXD, as a constant false-alarm rate (CFAR) adaptive anomaly detector, is derived from the generalized-likelihood ratio test [13]. However, RXD has two main limitations. First and foremost, while using local or global information to estimate background information, the samples might contain anomalies or noise. On the one hand, if the background statistics are estimated with anomalous samples, these are supposed to be far away from background samples on spectral space. These anomalies may be missed as they have a small RXD value. On the other hand, if the background statistics are estimated with noise samples (which can be considered outliers), the RXD value of the background will be higher. In both cases, the difference (in terms of RXD value) between anomalies and background is reduced [8]. Another problem is related to the normal distribution assumption as, in most cases, the normal distribution does not hold in real hyperspectral data [11].

Recently, several methods have been proposed to improve the estimation of background statistics for enhanced anomaly detection. In [12], an iterative method called locally adaptable iterative RX (LAIRX) is developed. It refines $\boldsymbol{\Sigma}$ and $\boldsymbol{\mu}$ by removing anomalous pixels from the background in order to improve the performance of the detector. However, the empirical threshold value needed for this purpose is very crucial for the performance and it is defined using a manual procedure. In [13], a kernel RX (KRX) method is presented, which maps the data into a higher dimensional feature space. It is shown that, in such kernel space, the data tend to follow a multivariate normal distribution. However, KRX has high computational complexity and can be affected by target interference. In [14], a dual-window approach was explored in order to model the local background around each PUT and reduce interference. However, this approach generally requires prior knowledge about the size of anomalies, which may not be available. In [15], an orthogonal subspace projection (OSP) approach for anomaly detection was proposed. After the OSP projection, the data were shown to be closer to a normal distribution. However, OSP can be quite sensitive to noise. More recently, a segment-based RXD (SRXD) has been developed which models the background using the mean vector and the covariance matrix of the cluster to which a given pixel belongs to [16]. A general observation is that a better estimation of

the covariance matrix generally improves the performance. However, in order to successfully apply the SRXD, it is required that the number of pixels in the cluster is greater or equal than the number of spectral bands in the hyperspectral data, so that the inverse of the covariance matrix can be calculated. This assumption may not hold in certain scenarios, particularly for small clusters. In the following section, we describe two new strategies to improve the characterization of background statistics for enhanced anomaly detection in hyperspectral data.

III. W-RXD AND LF-RXD

A. W-RXD

In order to reduce the impact of anomalous/noisy background pixels and improve the estimation of covariance matrix, W-RXD assigns different weights to the background samples. In the conventional RXD, when we calculate Σ and μ, the weight of each pixel is the same, i.e., $\frac{1}{N}$, where N is the number of considered samples. In order to retain background signal and reduce non-background signal, the W-RXD assigns those pixels that are close to the background a higher weight than the weight assigned to pixels that are far away from the background. As shown in (3), $p(\mathbf{x}|H_0)$ is the probability of the PUT being part of the background. Because the spectral signatures of anomalies that can be detected by RXD are supposed to be different to the spectral signatures of background samples [1], the anomaly has a small probability to be labeled as a background sample. This means that the weights assigned to anomalies are lower than the weights assigned to background samples. On the other hand, noisy pixels can be detected by RXD as outliers because they are similar to anomalies, with spectral signature which are very different with regards to the spectral signatures of background samples. As a result, the value of (3) for noisy pixels is small, which also indicates that noisy pixels have a small weight. Therefore, the background statistics estimation will contain few anomalous or noisy signatures when $p(\mathbf{x}|H_0)$ is used to properly weight the background covariance matrix and mean vector. In order to validate the use of $p(\mathbf{x}|H_0)$ as a group of probabilities, we first normalize $p(\mathbf{x}|H_0)$ as follows:

$$\hat{p}(\mathbf{x}_k|H_0) = p(\mathbf{x}_k|H_0)/\sum_{i=1}^{N} p(\mathbf{x}_i|H_0), \quad (k = 1, 2, \ldots, N).$$

$$(7)$$

After normalization, $\hat{p}(\mathbf{x}|H_0)$ can be used to weight the mean vector $\hat{\mu}$ and the covariance matrix $\hat{\Sigma}$ as follows:

$$\hat{\mu} = \sum_{i=1}^{N} \hat{p}(\mathbf{x}_i|H_0)\,\mathbf{x}_i \qquad (8)$$

and

$$\hat{\Sigma} = \sum_{i=1}^{N} \hat{p}(\mathbf{x}_i|H_0)(\mathbf{x}_i - \hat{\mu})(\mathbf{x}_i - \hat{\mu})^T \qquad (9)$$
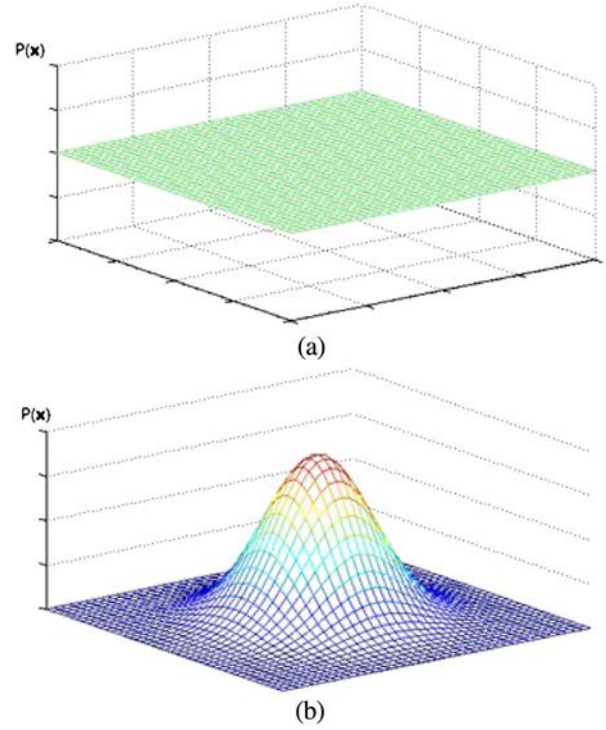

Fig. 1. (a) Weight assignment to samples by RXD and (b) weight assignment to samples by W-RXD.

where $\mathbf{x}_i$ denotes the ith pixel. After obtaining the new $\hat{\Sigma}$ and $\hat{\mu}$, the W-RXD can be simply defined as follows:

$$D_{W\text{-}RXD}(\mathbf{x}) = (\mathbf{x} - \hat{\mu})^T \hat{\Sigma}^{-1} (\mathbf{x} - \hat{\mu}). \qquad (10)$$

Fig. 1 illustrates the difference between the weights assigned by the conventional RXD and the ones considered by the proposed W-RXD. As it can be observed from Fig. 1, the proposed W-RXD assigns different weights to pixels according to their spectral distance from the background cluster. In the spectral domain, if the pixel is far away from the background, it will receive a small weight in the background estimation. In turn, RXD assigns the same weight to all pixels. With different weights, the anomalous signals and noise are reduced in the process of estimating the background, and the background is closer to a multivariate normal distribution.

B. LF-RXD

LFs have been widely used in signal processing and achieved good performance in many practical applications [17]. Based on linear filtering concepts, LF-RXD uses $p(\mathbf{x}|H_0)$ as a filter to retain background signals as follows:

$$\hat{p}(\mathbf{x}_k|H_0) = p(\mathbf{x}_k|H_0) \times N/\sum_{i=1}^{N} p(\mathbf{x}_i|H_0), \quad (k = 1, 2, \ldots, N)$$

$$(11)$$

$$\overline{\mathbf{x}}_i = \mathbf{x}_i \times \hat{p}(\mathbf{x}_i|H_0), \quad (i = 1, 2, \ldots, N). \qquad (12)$$

Notice that this step is intended to make sure that $\overline{\mathbf{x}}$ has the same scale as the original data, such that the result of LF-RXD

is chi-square distributed based on the Gaussian assumption. As a result, the mean vector and the covariance matrix of the background can be simply estimated as follows:

$$\overline{\boldsymbol{\mu}} = \sum_{i=1}^{N} \frac{\overline{\mathbf{x}}_i}{N} \tag{13}$$

$$\overline{\boldsymbol{\Sigma}} = \sum_{i=1}^{N} \frac{1}{N-1}(\overline{\mathbf{x}}_i - \overline{\boldsymbol{\mu}})(\overline{\mathbf{x}}_i - \overline{\boldsymbol{\mu}})^T \tag{14}$$

$$D_{LF\text{-}RXD}(\mathbf{x}) = (\mathbf{x} - \overline{\boldsymbol{\mu}})^T \overline{\boldsymbol{\Sigma}}^{-1}(\mathbf{x} - \overline{\boldsymbol{\mu}}). \tag{15}$$

Our introspection is that, after the linear filtering process, $\overline{\boldsymbol{\Sigma}}$ and $\overline{\boldsymbol{\mu}}$ represent more accurately the background information. This is because LF-RXD assigns the sample a scale value, which is decided by its probability of being part of the background. If the sample is far away from the background, a small scale value will be used to compress its signal in $\overline{\boldsymbol{\Sigma}}$ and $\overline{\boldsymbol{\mu}}$. On the contrary, a large scale value is used to magnify its signal as the sample contains abundant background information. The background samples estimated by LF-RXD are more different with regards to anomalies; therefore the anomalies are more likely to be actually outlier pixels in the original hyperspectral image. An experimental evaluation of the two aforementioned algorithms using synthetic data follows.

IV. SYNTHETIC DATA EXPERIMENTS

In this section, we use synthetic data to evaluate the newly developed methods. For this purpose, we use a target implantation strategy that has been successfully used for performance evaluation in previous developments [19]–[21]. The results are evaluated using receiver operating characteristic (ROC) curves [22] and the area under such curves (AUC) [20], which are common metrics for detection evaluation. In the following, we describe the procedure adopted for the generation of the synthetic data used in our experiments, as well as the evaluation results obtained.

A. Synthetic Data

The synthetic data were generated using the target detection blind-test scenes provided by Rochester Institute of Technology (RIT) [18]. These data were collected by a HyMap instrument over Cook City in Montana, on July 2006. The selected portion (illustrated in Fig. 2) has 280×800 pixels in size and 126 spectral bands. The spatial resolution of the data is quite fine, with a pixel size of approximately 3 m.

In this work, we have decided to use a target implantation method to simulate a set of anomalous targets in the considered hyperspectral data set over Cook City in Montana. The advantage of using a target implantation method is that we can evaluate the performance of the detectors in a totally controlled environment [19]. Our method generates the anomalous targets using a synthetic spectral signature $\mathbf{z}$ with a specified abundance fraction f from a desired target $\mathbf{t}$, contaminated by a background signature $\mathbf{b}$, in the spatial position in which the target of interest is simulated [20], [21]. This means that the implanted targets are all

Fig. 2. Hymap hyperspectral image over Cook City. Montana, with 20 embedded targets in a region called ROI-1.
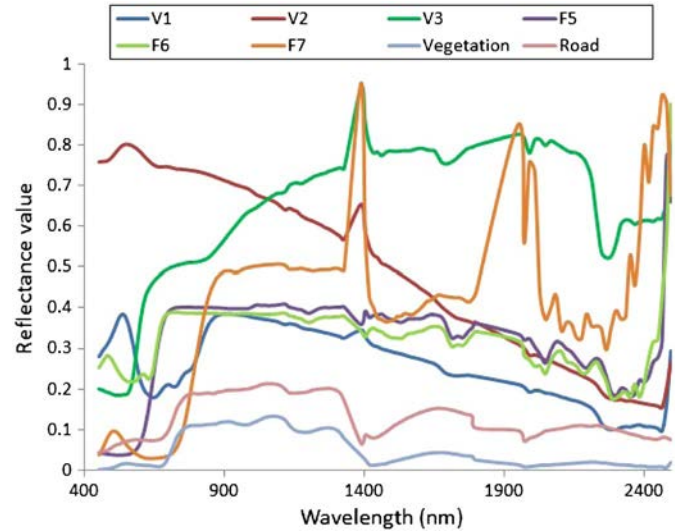

Fig. 3. Spectral signatures of the six targets implanted in the image and two types of backgrounds.

TABLE I
CHARACTERISTICS OF THE IMPLANTED TARGET SPECTRA IN OUR SYNTHETIC DATA EXPERIMENTS

Name	Type
V1	1993 Chevy Blazer
V2	1997 Toyota T100
V3	1985 Subaru GL Wagon
F5	Maroon Nylon Target
F6	Gray Nylon Target
F7	Green Cotton Target

sub-pixel in nature. For the simulations, we use a simple linear mixture model as follows:

$$\mathbf{z} = f \cdot \mathbf{t} + (1 - f) \cdot \mathbf{b}. \tag{16}$$

Fig. 3 shows the spectral signatures of the six targets (corresponding to different man-made materials present in different locations of the scene, as provided by the target detection blind-test scenes provided by RIT) that have been implanted in the hyperspectral scene, together with two considered background signatures. The image portion where the targets have been implanted is denoted as ROI-1 (see Fig. 2), which is an open vegetation region with dimensions $100 \times 100 \times 126$ and contains few anomalous pixels. Vegetation can be considered as the
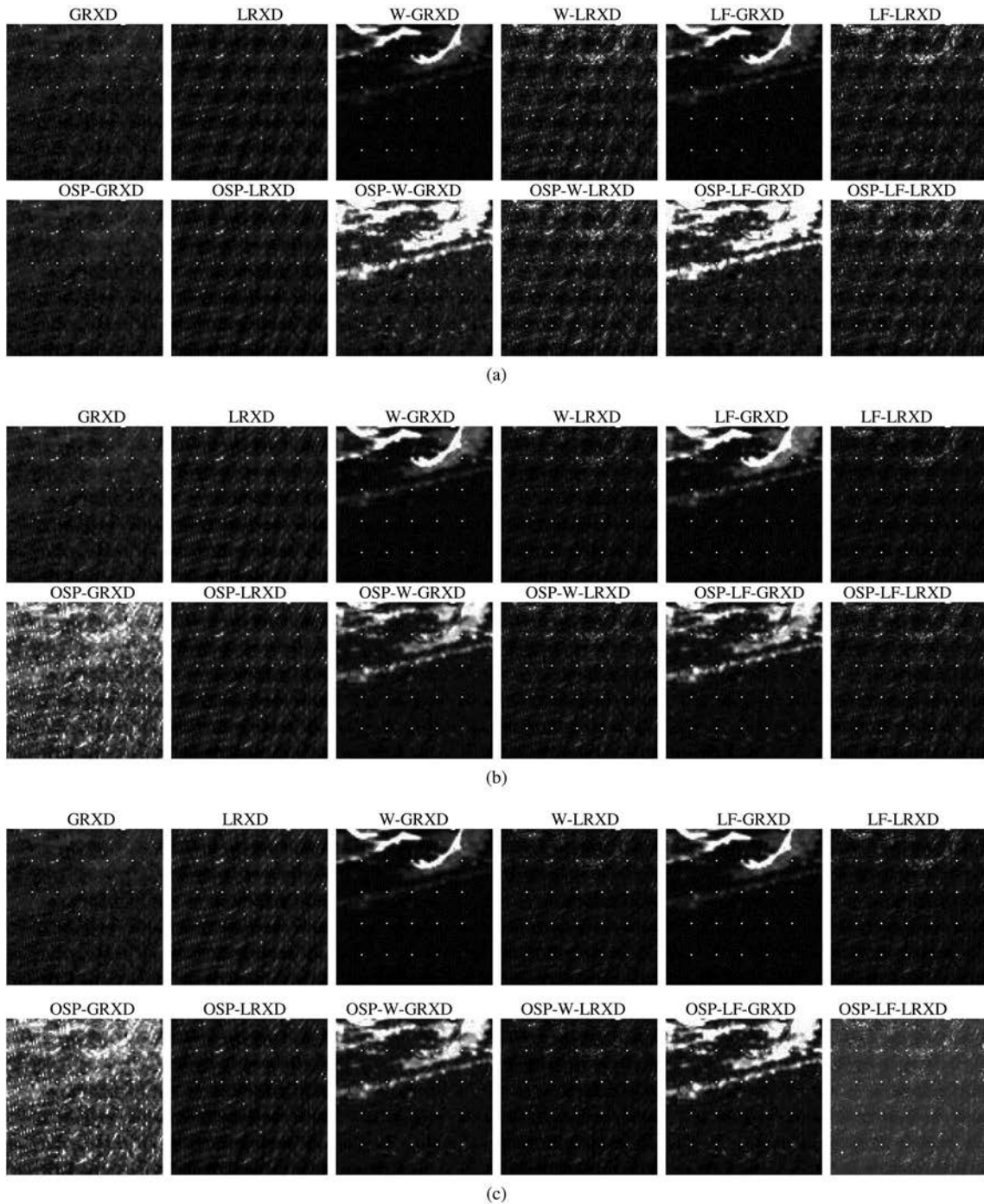
Fig. 4. Detection results provided by different algorithms on the synthetic data with implanted anomalous targets: (a) V1, (b) V2, (c), V3 (d) F5, (e) F6, and (f) F7.

main homogeneous background in this region. In order to evaluate the presented method, we use six kinds of targets that have been implanted into ROI-1 using (16), where the characteristics of the targets are summarized on Table I. We have synthetically generated six different test images, where each image contains only one type of target with different fractions. In each test image, 4×5 targets have been implanted, where the abundance fractions f follow an arithmetic progression with difference of 0.02 from left to right and top to bottom, and where the maximum value is 0.4 on the top-left target, and the minimum value is 0.02 on the bottom-right target. The main

reason why we set 0.4 as the maximum value of f is that, when f is higher than 0.4, there are no false alarms when the target is detected. We decided to set the common difference as 0.02 since we would like to make a complete evaluation of the capability of the detectors with a sufficiently small difference of the target abundance f.

B. Preliminary Evaluation

This section presents the experimental results obtained by the discussed approaches, implemented using global (W-GRXD, LF-GRXD) and local (LF-LRXD, W-LRXD). W-GRXD uses
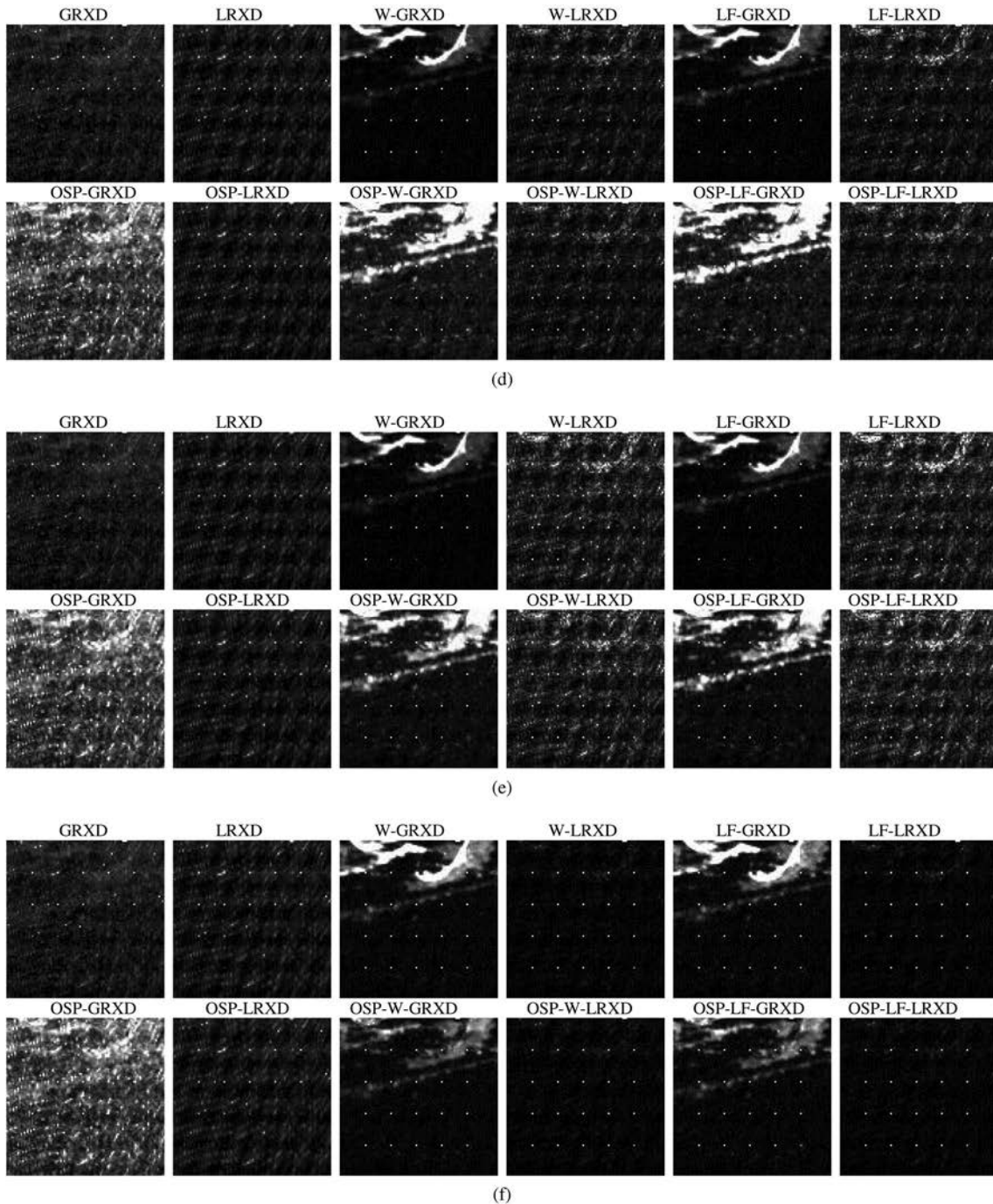
Fig. 4. *(Continued)*

all pixels with different weights to estimate the statistics of the background, while W-LRXD uses local pixels to perform such estimation. LF-GRXD and LF-LRXD are similar to GRXD and LRXD, except by the fact that these methods preprocess the image by using LF. For comparative purposes, we also included the methodology described in [15] which first performs OSP processing to adapt the hyperspectral data to a normal distribution, and then applies all the aforementioned RXD variants. The window size of the local methods was empirically set to 3×3 since it was observed experimentally that this parameter setting leads to the best results in our experiments. For illustrative purposes, Fig. 4 presents the detection results of the 12

considered algorithms, while Fig. 5 shows the binary images obtained after applying an empirical threshold to the obtained detection results.

As Fig. 4 shows, the implanted targets can be better detected by W-RXD and LF-RXD (independently of the application of OSP preprocessing). This observation is confirmed by the results presented in Fig. 5, which have been obtained by setting a constant ratio of anomaly, obtaining a set of binary images that can be used as an indication to evaluate the performance of the different compared algorithms.

Several conclusions can be obtained from Fig. 5. First and foremost, OSP-W-GRXD and OSP-LF-GRXD can detect on
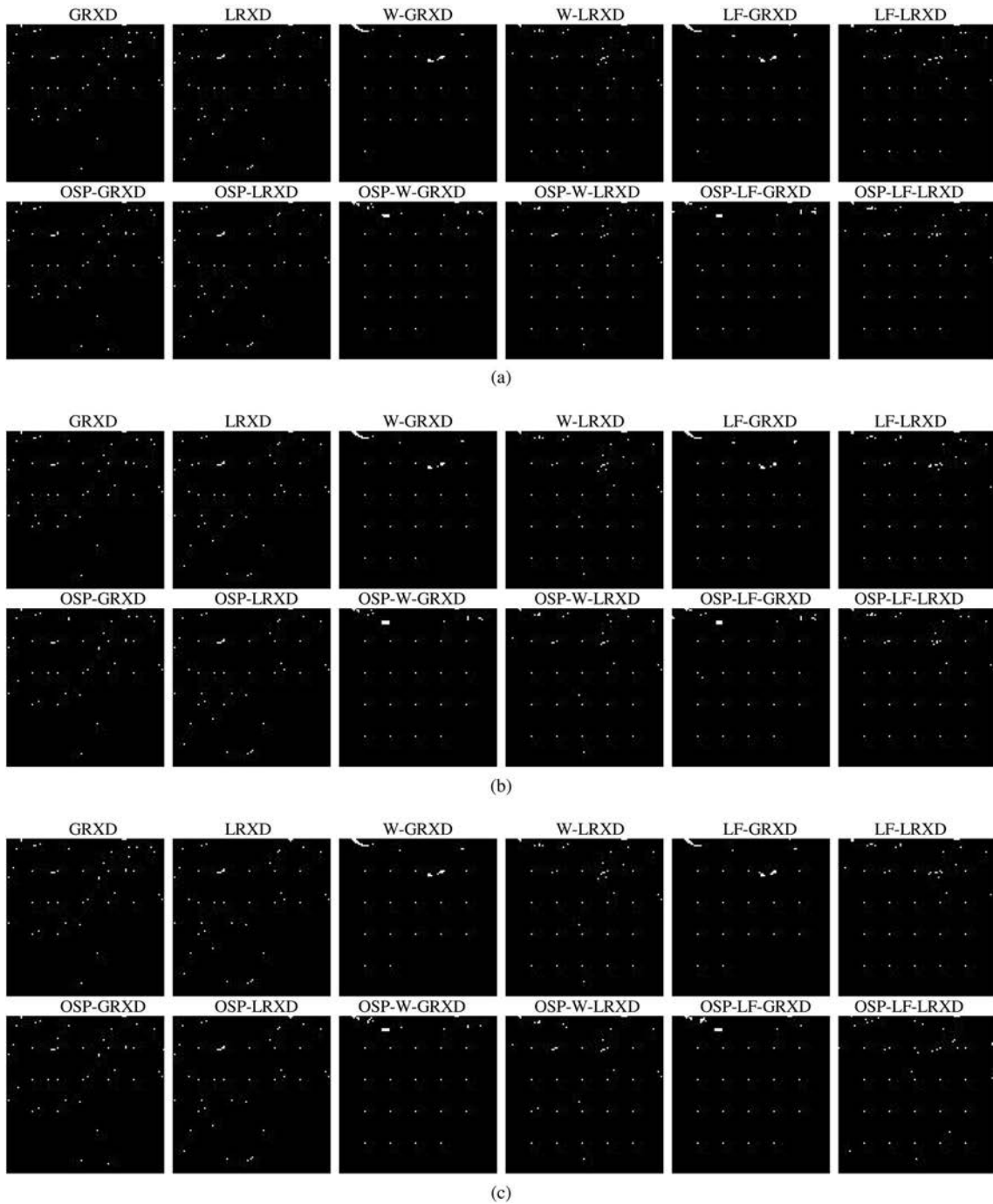
Fig. 5. Binary images obtained after thresholding the detection results provided of different anomaly detection algorithms: (a) V1, (b) V2, (c), V3 (d) F5, (e) F6, and (f) F7.

average more targets (about 18 out of the total 20 implanted ones), whereas OSP-GRXD can only detect 12 of them. Moreover, without OSP, W-GRXD and LF-GRXD can detect about 16 implanted targets, whereas GRXD can only detect 12, the same as OSP-GRXD. For instance, for V2 both OSP-W-GRXD and OSP-LF-GRXD can detect the targets with f equal or higher than 0.04. W-GRXD and LF-GRXD can detect the targets with f equal or higher than 0.06. However, both OSP-GRXD and GRXD can only detect the targets with f equal or higher than 0.18. This indicates that W-RXD and LF-RXD can detect the

anomalous targets with less abundance in the pixel, regardless of the OSP preprocessing. Furthermore, it is noticeable that W-RXD and LF-RXD lead to qualitatively less false alarms as the other tested methods. As can be observed in Fig. 5, the results of the classic RXD reveal several isolated points as false alarms, which are mainly caused by noise, illumination variation on the background, etc. As a result, it can be concluded that the proposed methods reduce such false alarms significantly. It can also be observed that the presented methods generally provide false alarm regions rather than isolated pixels. This kind of false
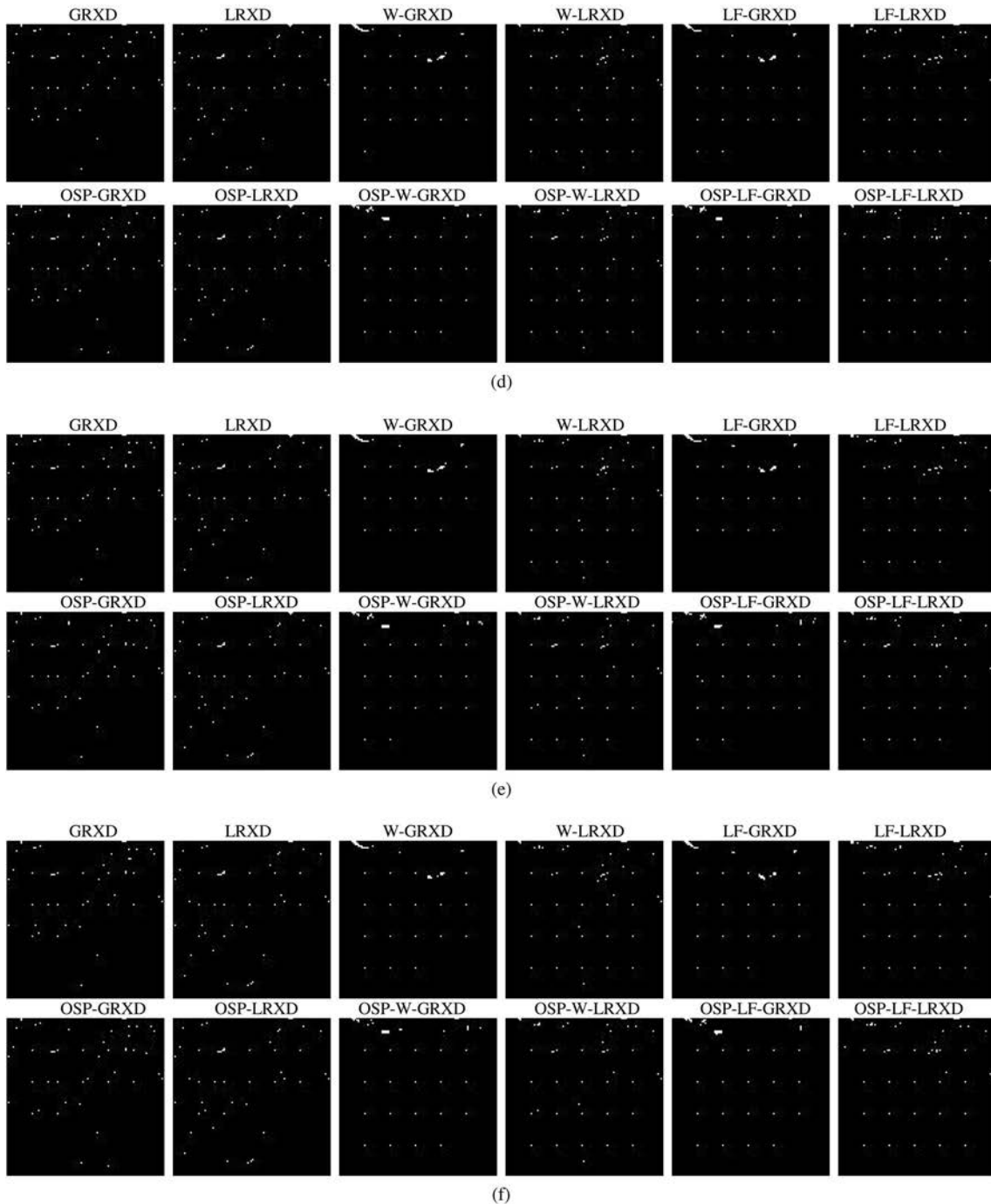
Fig. 5. *(Continued)*

alarm can be more easily rejected than individual pixels, for instance using shape characteristics.

C. ROC Analysis

ROC curves provide an essential metric for quantitative evaluation of detection performance. This type of curves establishes a one-to-one correspondence between the true positive rate and the false alarm rate (FAR) in the detection process, using different thresholds. As a result, the ROC curves allow for a detailed quantitative evaluation of the detector independently of subjective thresholds. Fig. 6 shows the ROC curves

corresponding to the detection results reported in Fig. 4. The more the AUC, the better the detection results. It is remarkable that, in comparison with the conventional RXD, our proposed methods W-RXD and LF-RXD improve the true positive detection rate while reducing the FAR. In other words, both W-RXD and LF-RXD resulted in lower FAR when compared with the RXD for a similar true positive rate. On the other hand, OSP-W-RXD and OSP-LF-RXD achieve better performance than W-RXD and LF-RXD, while OSP-RXD and RXD have the almost same detection capability on all test images. Since OSP implements a linear transformation to the data and linear
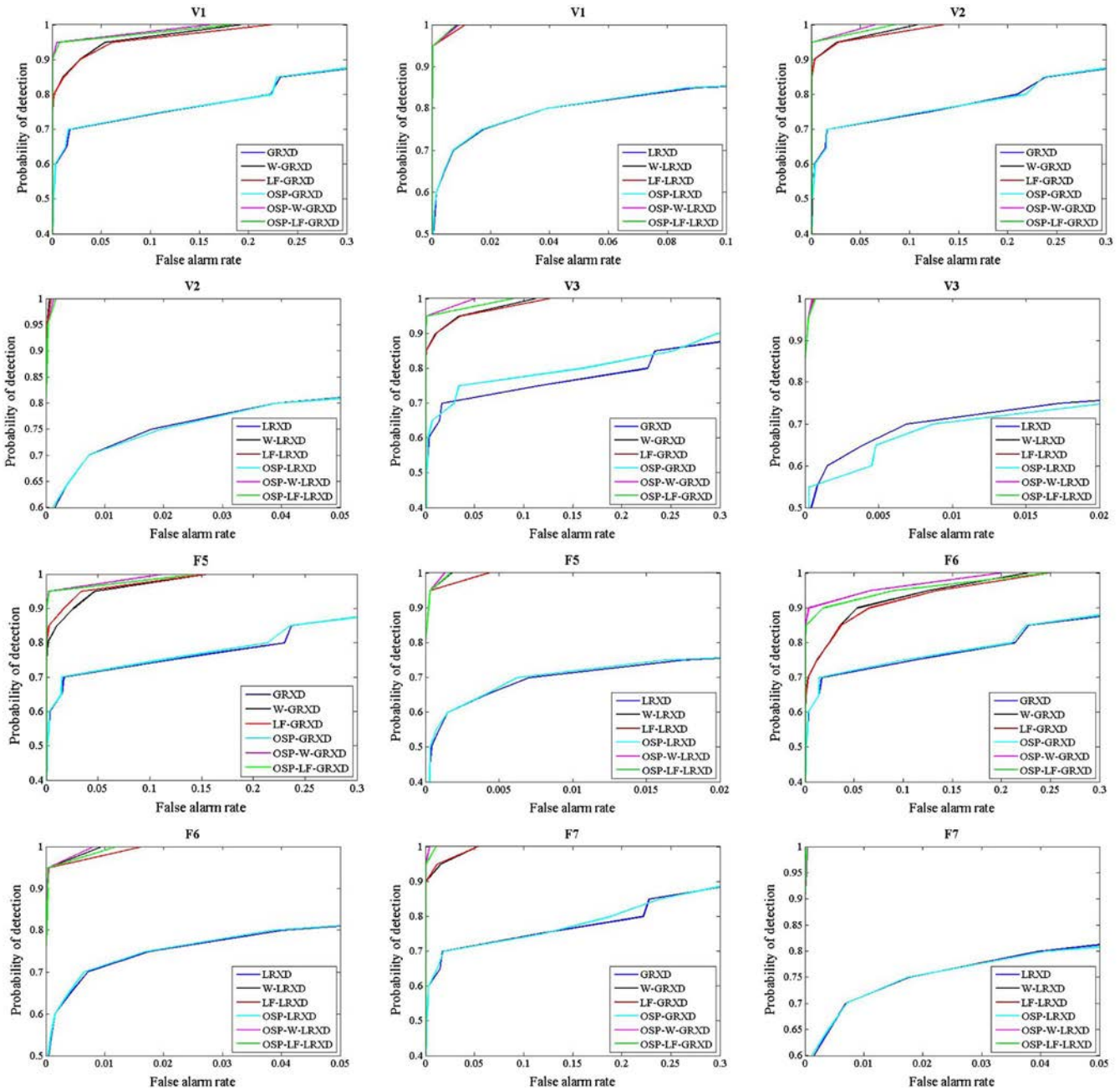
Fig. 6. ROC curves corresponding to the detection results reported in Fig. 4.

transformation has no influence on the RXD value, the ROC curves of RXD and OSP-RXD are very similar. However, as W-RXD uses different weight to calculate the covariance matrix and LF-RXD filters the data by a LF, the linear transformation impacts the final results and all ROC curves indicate that OSP-W-RXD is most effective among the considered detectors. Furthermore, Table II indicates that the local-based methods LRXD, W-LRXD, and LF-LRXD generally provide noticeably higher AUC than global methods (GRXD, W-GRXD, and LF-GRXD). This is mainly because all the targets that we implanted are sub-pixel in size, hence local pixels tend to represent the background better. This scenario is quite common in practice, since in many cases the spatial resolution of the hyperspectral sensor is not enough to totally separate the targets from the background and many targets (especially anomalous ones) are sub-pixel in nature.

V. REAL IMAGE EXPERIMENTS

In this section, two real hyperspectral data collected by different instruments have been used for experimental evaluation of the newly proposed detectors in different real scenarios. In these experiments with real data, we also included LAIRX in order to provide a more detailed comparison of the proposed algorithms with regards to other established methods. The two considered scenes contain ground-truth information, which has been used for the evaluation. In the following, we provide a description of the considered data sets.

TABLE II
AUC FOR THE DETECTORS REPORTED IN FIGS. 4–6

| Target	Algorithm	AUC	Algorithm	AUC	Algorithm	AUC
V1	GRXD	0.9079	W-GRXD	0.9905	LF-GRXD	0.9893
	LRXD	0.9422	W-LRXD	0.9997	LF-LRXD	0.9997
	OSP-GRXD	0.9099	OSP-W-GRXD	0.9958	OSP-LF-GRXD	0.9950
	OSP-LRXD	0.9431	OSP-W-LRXD	0.9997	OSP-LF-LRXD	0.9998
V2	GRXD	0.9098	W-GRXD	0.9959	LF-GRXD	0.9951
	LRXD	0.9420	W-LRXD	1.0000	LF-LRXD	1.0000
	OSP-GRXD	0.9104	OSP-W-GRXD	0.9984	OSP-LF-GRXD	0.9979
	OSP-LRXD	0.9447	OSP-W-LRXD	0.9999	OSP-LF-LRXD	0.9999
V3	GRXD	0.9114	W-GRXD	0.9950	LF-GRXD	0.9945
	LRXD	0.9455	W-LRXD	1.0000	LF-LRXD	1.0000
	OSP-GRXD	0.9168	OSP-W-GRXD	0.9987	OSP-LF-GRXD	0.9977
	OSP-LRXD	0.9452	OSP-W-LRXD	1.0000	OSP-LF-LRXD	1.0000
F5	GRXD	0.9100	W-GRXD	0.9919	LF-GRXD	0.9935
	LRXD	0.9446	W-LRXD	0.9999	LF-LRXD	0.9999
	OSP-GRXD	0.9112	OSP-W-GRXD	0.9970	OSP-LF-GRXD	0.9962
	OSP-LRXD	0.9446	OSP-W-LRXD	0.9999	OSP-LF-LRXD	0.9999
F6	GRXD	0.9105	W-GRXD	0.9816	LF-GRXD	0.9799
	LRXD	0.9446	W-LRXD	0.9997	LF-LRXD	0.9995
	OSP-GRXD	0.9125	OSP-W-GRXD	0.9915	OSP-LF-GRXD	0.9883
	OSP-LRXD	0.9434	OSP-W-LRXD	0.9998	OSP-LF-LRXD	0.9997
F7	GRXD	0.9127	W-GRXD	0.9979	LF-GRXD	0.9981
	LRXD	0.9438	W-LRXD	1.0000	LF-LRXD	1.0000
	OSP-GRXD	0.9145	OSP-W-GRXD	0.9999	OSP-LF-GRXD	0.9997
	OSP-LRXD	0.9423	OSP-W-LRXD	1.0000	OSP-LF-LRXD	1.0000
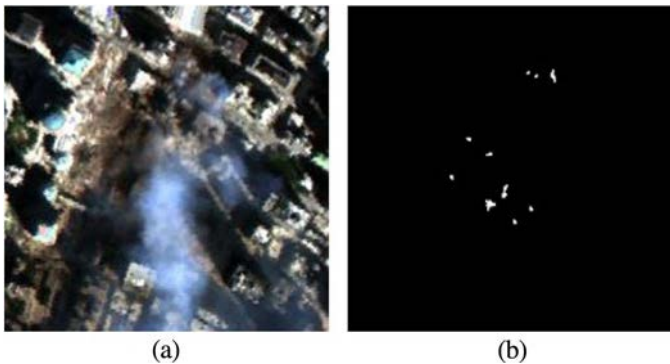
Fig. 7. (a) AVIRIS image over the World Trade Center in New York City and (b) ground-truth map indicating the spatial location of hot spot fires, available from the USGS.
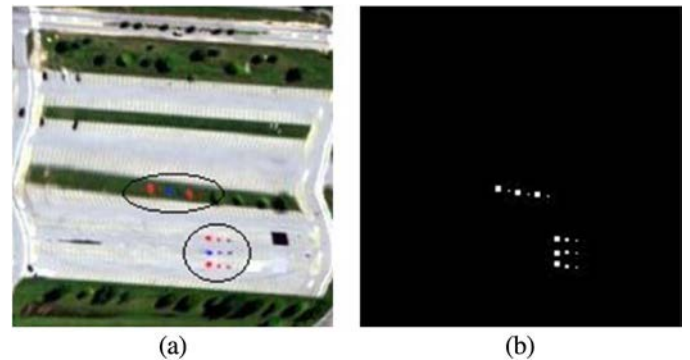

Fig. 8. (a) SpecTIR hyperspectral image with the targets highlighted by black ellipses and (b) ground-truth information.

A. Real Data Description

1) World Trade Center: This data set was collected by the airborne visible Infra-Red Imaging Spectrometer (AVIRIS), operated by NASA's Jet Propulsion Laboratory, over the World Trade Center (WTC) area in New York, on September 16, 2001 (just 5 days after the terrorist attacks that collapsed the two main towers in the WTC complex) [23]. A portion of 200×200 pixels (with 224 spectral bands between 0.4 and 2.5 µm) was selected for the experiments. This area covered the hot spots corresponding to latent fires at the WTC, which can be considered as anomalies. Fig. 7(a) shows a false color representation of the portion selected for experiments, while Fig. 7(b) displays a ground-truth data, which comprises the spatial location of the hot spots provided by the United States Geological Survey (USGS).

2) SpecTIR Data: This image was obtained from a data collection campaign called SpecTIR hyperspectral airborne Rochester experiment (SHARE) [24]. The data set was collected on July 29, 2010 by the ProSpecTIR-VS2 sensor and comprises 360 bands from 390 to 2450 nm with 5 nm spectral resolution. The pixel size is approximately 1 m. In the considered hyperspectral scene, road and vegetation are the main backgrounds and the targets are several red and blue fabrics with size of 9, 4, and $0.25\ \mathrm{m}^2$, respectively. In our experiments, we selected an area of 180×180 pixels which contains several targets as indicated in Fig. 8(a). The ground-truth location of the targets is also available and displayed in Fig. 8(b). Since the data is quite noisy, we decided to downsize it to 120 spectral bands by averaging each three neighboring spectral bands into one single band.
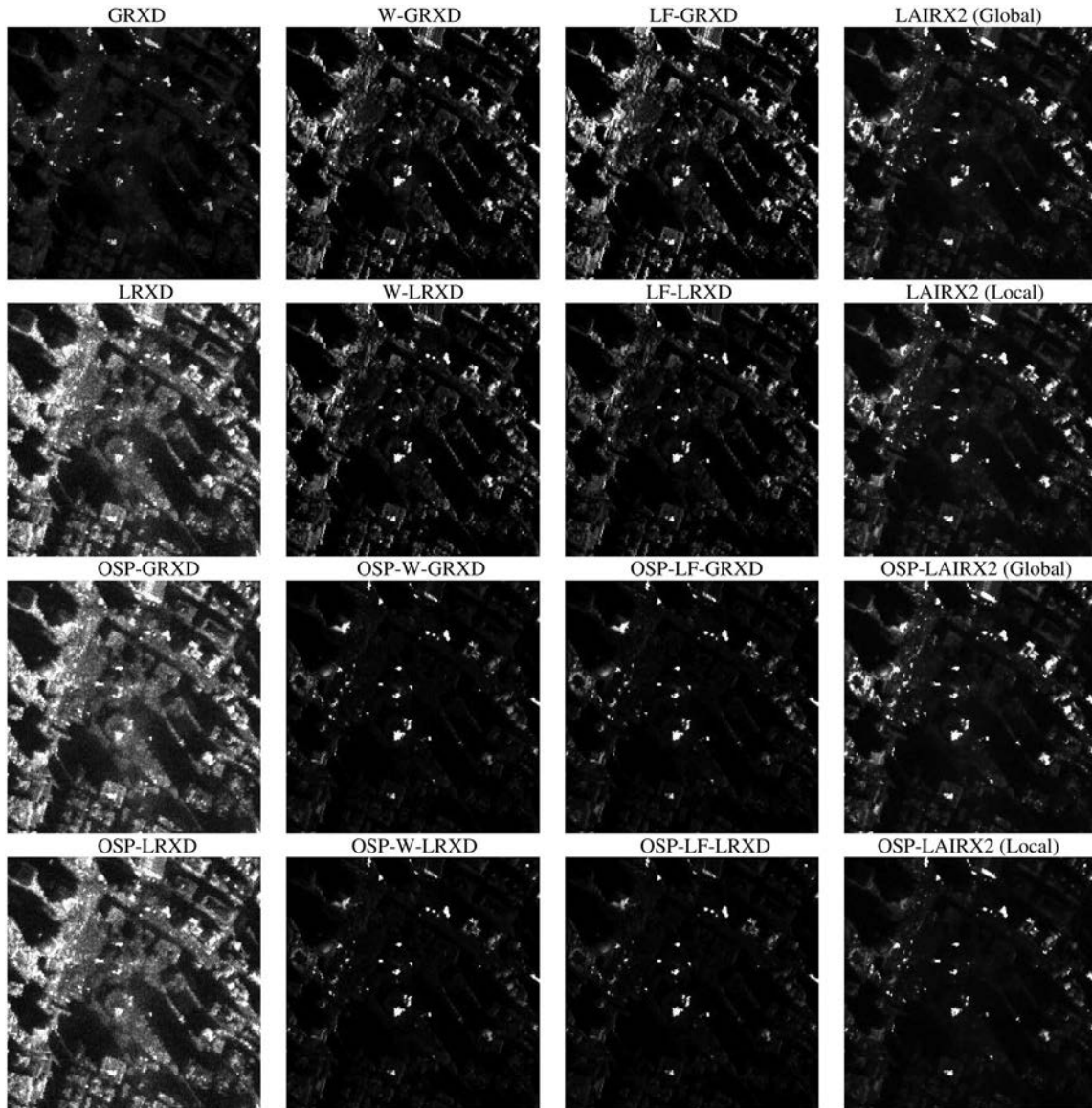
Fig. 9. Detection results obtained by different algorithms for the AVIRIS World Trade Center data.
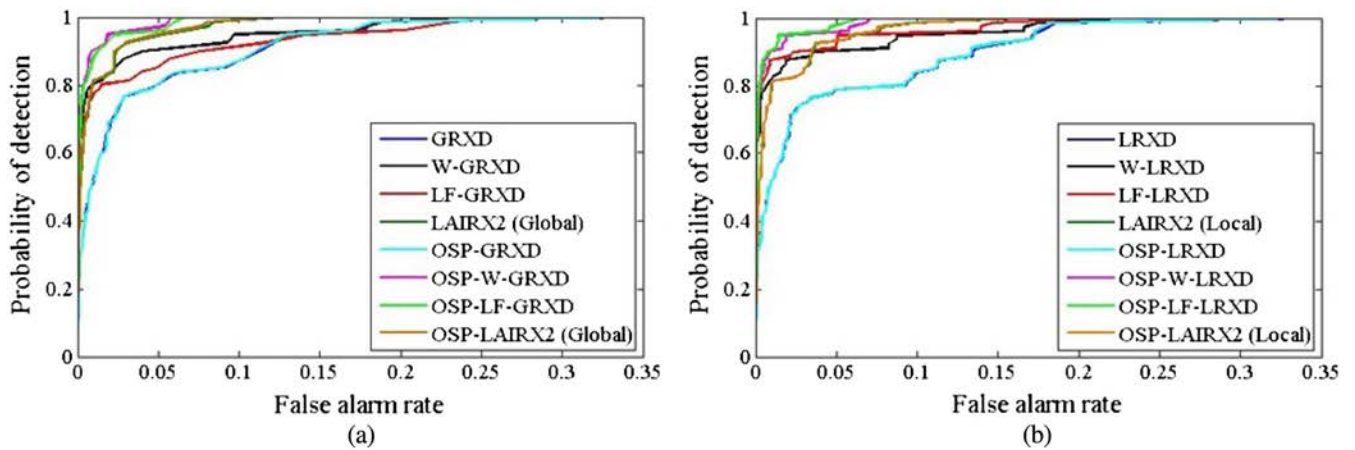

Fig. 10. ROC curves corresponding to the detection results described in Fig. 9: (a) global methods and (b) local methods.

TABLE III
AUC FOR THE DETECTORS REPORTED IN FIGS. 9 AND 10

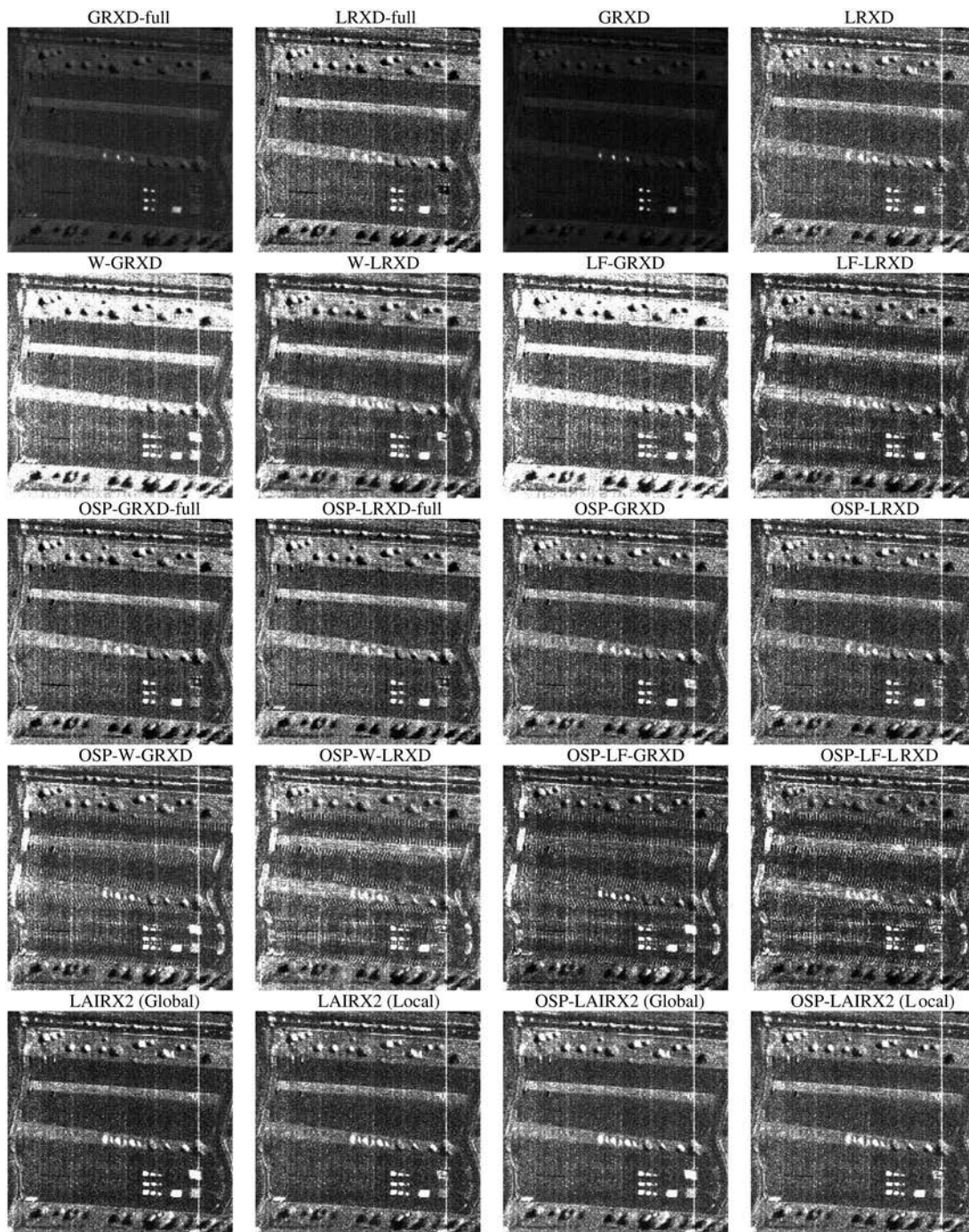| Algorithm	AUC	Algorithm	AUC	Algorithm	AUC	Algorithm	AUC
GRXD	0.9689	LRXD	0.9638	OSP-GRXD	0.9692	OSP-LRXD	0.9642
W-GRXD	0.9837	W-LRXD	0.9856	OSP-W-GRXD	0.9956	OSP-W-LRXD	0.9955
LF-GRXD	0.9772	LF-LRXD	0.9895	OSP-LF-GRXD	0.9951	OSP-LF-LRXD	0.9963
LAIRX2 (Global)	0.9905	LAIRX2 (Local)	0.9888	OSP-LAIRX2 (Global)	0.9909	OSP-LAIRX2 (Local)	0.9890

Fig. 11. Detection results obtained by different algorithms for the SpecTIR data.
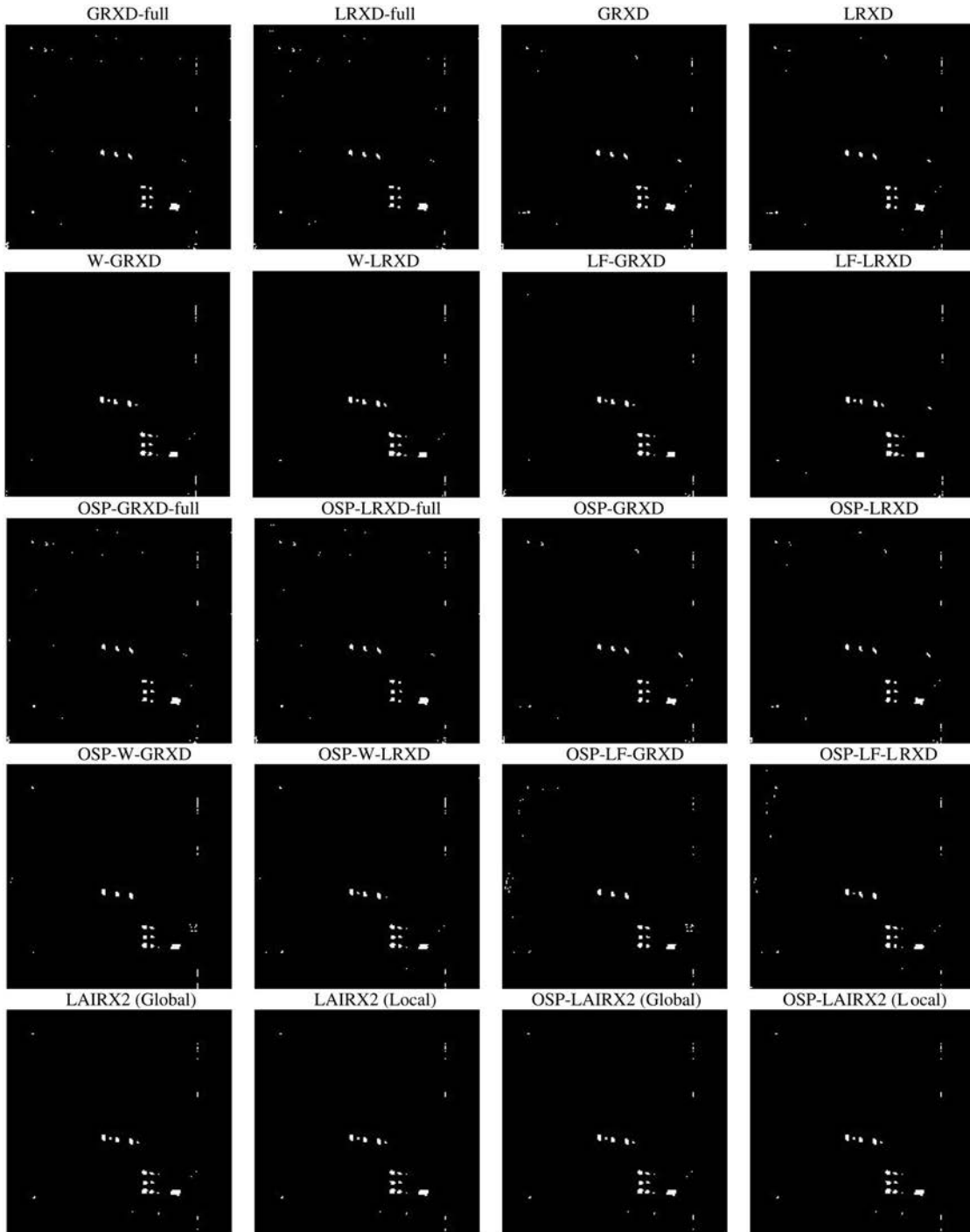
Fig. 12. Binary images obtained from the detection results in Fig. 11.

B. Experimental Results

As the size of the targets in these two images is usually more than one pixel, the local methods in the experiments have been implemented using a dual window approach [14] to better estimate the background information. The inner and the outer window sizes of the dual window are set to 5×5 and 15×15, respectively, considering the size of the targets.

1) World Trade Center: The detection results obtained after applying the proposed methods to the WTC hyperspectral data set are reported in Fig. 9. We provide a comparison between our

methods and LAIRX for further comparison. Considering that both W-RXD and LF-RXD calculate RX value twice, we use LAIRX2 that only does 2 RX-type iterations [12]. We also use two models (global and local) in LAIRX2 for the estimation of background. The threshold in LAIRX2 is set as $\chi^2_{0.001, \, K}$ (K is the number of bands), considering the proportion of targets in the image. In general, we can observe that the proposed methods and LAIRX2 algorithms detected the targets with less false alarms than GRXD and LRXD. The proposed methods improved after the data was processed by OSP, while OSP could not
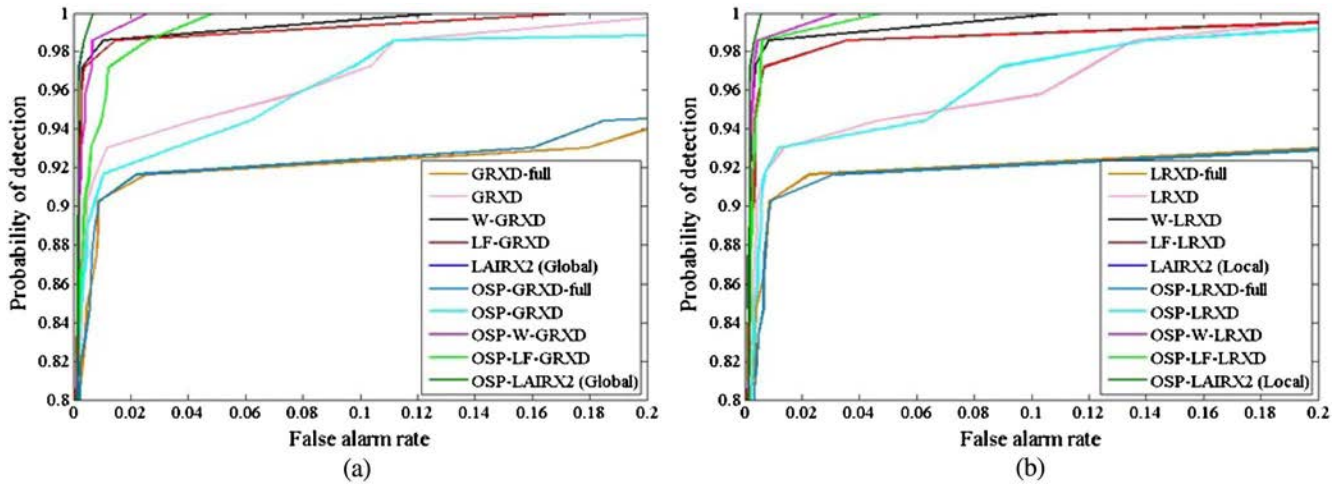
Fig. 13. ROC curves corresponding to the detection results reported in Fig. 11: (a) global methods and (b) local methods.

TABLE IV
AUC FOR THE DETECTORS REPORTED IN FIGS. 11–13

Algorithm	AUC	Algorithm	AUC	Algorithm	AUC	Algorithm	AUC
GRXD-full	0.9683	LRXD-full	0.9651	OSP-GRXD-full	0.9699	OSP-LRXD-full	0.9648
GRXD	0.9929	LRXD	0.9919	OSP-GRXD	0.9896	OSP-LRXD	0.9918
W-GRXD	0.9986	W-LRXD	0.9987	OSP-W-GRXD	0.9992	OSP-W-LRXD	0.9993
LF-GRXD	0.9982	LF-LRXD	0.9970	OSP-LF-GRXD	0.9983	OSP-LF-LRXD	0.9990
LAIRX (Global)	0.9996	LAIRX (Local)	0.9996	OSP-LAIRX (Global)	0.9996	OSP-LAIRX (Local)	0.9996

make an improvement with regards to the standard RXD and LAIRX2.

OSP-W-RXD and OSP-LF-RXD can detect more real targets than LAIRX2 in this particular experiment. The corresponding ROC curves are reported on Fig. 10. Here, it can be seen that the proposed methods (either local or global) are significantly better than the original RXD. This is quantitatively confirmed by the AUC results reported on Table III, which indicate that the OSP-LF-LRXD outperforms all other detectors for this particular scene.

2) SpecTIR Data: Fig. 11 presents the detection results obtained for the SpecTIR data, with thresholded images (using empirical thresholds) reported in Fig. 12 for clarity. From Figs. 11 and 12, it is remarkable that the proposed methods can properly detect small anomalies that cannot be identified by the classic methods GRXD and LRXD. As it can be observed from Fig. 12, all methods can easily detect targets with sizes ranging between 9 and 4 m^2. However, for the 0.25 m^2 anomalous targets (of sub-pixel nature), W-RXD and LF-RXD are able to detect four sub-pixel targets out of six, while GRXD and LRXD could not detect any of them. This is an important observation, as it reveals that the presented methods exhibit better capacity to detect sub-pixel anomalies. Finally, it is also remarkable that the proposed methods always provided less isolated pixels as false alarms than both GRXD and LRXD. This indicates the W-RXD and LF-RXD have a better performance to suppress noise and reduce FAR in the considered data set.

For illustrative purposes, Fig. 13 presents the ROC curves corresponding to the detection results reported in Fig. 11. These curves, together with the AUC scores provided in

Table IV, reveal that W-GRXD, W-LRXD, LF-GRXD, and LF-LRXD have similar performance that is always superior to conventional RXD-based algorithms for all considered targets. As shown in Table IV, OSP preprocessing can enhance the performance of the proposed methods. The table also indicates that LAIRX2 algorithms (either global or local, OSP-based or not) exhibit the best overall performance among the considered methods.

Summarizing, the experiments conducted using both synthetic and real data sets indicate satisfactory performance of all the (local and global) methods presented in this contribution. Although LAIRX methods obtain very good performance with the SpecTIR data, the issue of how to decide the threshold value adaptively still needs to be addressed in future work. In fact, instead of using a rigid threshold value to separate anomalies from background as LAIRX does, W-RXD, and LF-RXD use a probability-based technique to estimate whether the sample pixel belongs to the background or not. As a result, we believe that W-RXD and LF-RXD can be more adaptive in the task of refining the background statistics information than LAIRX. On the other hand, the OSP preprocessing can adapt the hyperspectral data to a normal distribution. However, OSP did not work well when combined with the original RXD and LAIRX methods as the value of RXD was not changed when OSP performs a linear transformation to the data. On the contrary, OSP can improve the detection performance when combined with W-RXD and LF-RXD, as they use various weights or scales on different samples. All in all, the simple (yet powerful) algorithms developed in this work provide improved performance with regards to the original RXD-based counterparts (particularly, in terms of

reducing FAR) without significantly increasing computational complexity.

VI. CONCLUSION AND FUTURE RESEARCH LINES

The RXD has been widely used in the literature to perform anomaly detection in hyperspectral images. However, a crucial issue for the RXD is how to accurately characterize the background. In this paper, we have focused on this issue and further developed two simple (yet effective) variations of RXD, called W-RXD and LF-RXD. The main innovation of these two new algorithms with regards to the original RXD is the fact that they perform a more accurate estimation of the background statistics. Unlike the RXD, which uses a constant weight to model the statistics of background, W-RXD provides different weights for the pixels according to their background characteristics, so as to obtain a better balance between anomalies and background pixels in the detection process. In turn, the LF-RXD performs linear filtering prior to anomaly/noise characterization, with the ultimate goal of obtaining a better representation of background signals. Both methods aim at bringing the background distribution closer to a multivariate normal distribution, which is a main assumption of RXD. Our experimental results, conducted using both synthetic and real hyperspectral data sets, indicate that both W-RXD and LF-RXD (either in local and global versions) provide better performance than RXD, particularly for the detection of sub-pixel targets, particularly when combined with OSP preprocessing. Future work will be focused on the development of additional comparisons with other more sophisticated anomaly detection methods and also on developing more computationally efficient implementations of the newly developed methods, although the new methods presented in this contribution exhibit very similar computational complexity when compared with available methods.

ACKNOWLEDGMENTS

REFERENCES

[1] D. W. J. Stein, S. G. Beaven, L. E. Hoff, E. M. Winter, A. P. Schaum, and A. D. Stocker, "Anomaly detection from hyperspectral imagery," *IEEE Signal Process. Mag.*, vol. 19, pp. 58–69, Jan. 2002.

[2] C. I. Chang and S. S. Chiang, "Anomaly detection and classification for hyperspectral imagery," *IEEE Trans. Geosci. Remote Sens.*, vol. 40, pp. 1314–1325, Jun. 2002.

[3] C. I. Chang and D. C. Heinz, "Constrained subpixel target detection for remotely sensed imagery," *IEEE Trans. Geosci. Remote Sens.*, vol. 38, pp. 1144–1159, May 2000.

[4] W. H. Farrand and J. C. Harsanyi, "Mapping the distribution of mine tailings in the Coeur d'Alene River Valley, Idaho, through the use of a constrained energy minimization technique," *Remote Sens. Environ.*, vol. 59, pp. 64–76, Jan. 1997.

[5] H. Ren and C. I. Chang, "Target-constrained interference-minimized approach to subpixel target detection for hyperspectral images," *Opt. Eng.*, vol. 39, pp. 3138–3145, Dec. 2000.

[6] Q. Du and C. I. Chang, "A signal-decomposed and interference-annihilated approach to hyperspectral target detection," *IEEE Trans. Geosci. Remote Sens.*, vol. 42, pp. 892–906, Apr. 2004.

[7] I. S. Reed and X. Yu, "Adaptive multiple-band CFAR detection of an optical pattern with unknown spectral distribution," *IEEE Trans. Acoust. Speech Signal Process.*, vol. 38, pp. 1760–1770, Oct. 1990.

[8] B. Du and L. P. Zhang, "Random-selection-based anomaly detector for hyperspectral imagery," *IEEE Trans. Geosci. Remote Sens.*, vol. 49, pp. 1578–1589, May 2011.

[9] N. Billor, A. S. Hadi, and P. F. Velleman, "BACON: Blocked adaptive computationally efficient outlier nominators," *Comput. Statist. Data Anal.*, vol. 34, no. 3, pp. 279–298, 2000.

[10] N. Gorelnik, H. Yehudai, and S. R. Rotman, "Anomaly detection in non-stationary backgrounds," in *Proc. 2nd Workshop Hyperspectral Image Signal Process.: Evol. Remote Sens.* (WHISPERS 2010). Reykjavik, Iceland, Jun. 14–16, 2010.

[11] A. Banerjee, P. Burlina, and C. Diehl, "A support vector method for anomaly detection in hyperspectral imagery," *IEEE Trans. Geosci. Remote Sens.*, vol. 44, pp. 2282–2291, Aug. 2006.

[12] Y. Taitano, B. Geier, and K. Bauer, "A locally adaptable iterative RX detector," *EURASIP J. Adv. Signal Process.*, vol. 2010, p. 341908, 2010.

[13] H. Kwon and N. M. Nasrabadi, "Kernel RX-algorithm: A nonlinear anomaly detector for hyperspectral imagery," *IEEE Trans. Geosci. Remote Sens.*, vol. 43, pp. 388–397, Feb. 2005.

[14] H. Kwon, S. Z. Der, and N. M. Nasrabadi, "Adaptive anomaly detection using subspace separation for hyperspectral imagery," *Opt. Eng.*, vol. 42, pp. 3342–3351, Nov. 2003.

[15] L. Ma and J. W. Tian, "Anomaly detection for hyperspectral images based on improved RX algorithm—art. no. 67870Q," in *Mippr 2007: Multispectral Image Processing: Proc. SPIE*, H. Maitre, H. Sun, and J. Liu, Eds. Bellingham, WA, USA: SPIE–International Society for Optical Engineering, 2007, pp. Q7870–Q7870.

[16] C. E. Caefer, J. Silverman, O. Orthal, D. Antonelli, Y. Sharoni, and S. R. Rotman, "Improved covariance matrices for point target detection in hyperspectral data," *Opt. Eng.*, vol. 47, no. 7, pp. 076402–076413, Jul. 2008.

[17] S. M. Kay, *Fundamentals of Statistical Signal Processing, Volume 2: Detection Theory*. Englewood Cliffs, NJ, USA: Prentice-Hall, 1998, pp. 345–349.

[18] *Target Detection Blind Test* [Online]. Available: http://dirsapps.cis.rit.edu/blindtest/.

[19] S. M. Schweizer and J. M. F. Moura, "Efficient detection in hyperspectral imagery," *IEEE Trans. Image Process.*, vol. 10, pp. 584–597, Apr. 2001.

[20] S. Khazai, S. Homayouni, A. Safari, and B. Mojaradi, "Anomaly detection in hyperspectral images based on an adaptive support vector method," *IEEE Geosci. Remote Sens. Lett.*, vol. 8, pp. 646–650, Jul. 2011.

[21] M. S. Stefanou and J. P. Kerekes, "A method for assessing spectral image utility," *IEEE Trans. Geosci. Remote Sens.*, vol. 47, pp. 1698–1706, Jun 2009.

[22] M. T. Eismann, *Hyperspectral Remote Sensing*. Bellingham, WA, USA: SPIE Press, 2012, pp. 620–624.

[23] J. M. Molero, E. M. Garzon, I. Garcia, and A. Plaza, "Analysis and optimizations of global and local versions of the RX algorithm for anomaly detection in hyperspectral data," *IEEE J. Sel. Topics Appl. Earth Observ. Remote Sens.*, vol. 6, pp. 801–814, Apr. 2013.

[24] J. A. Herweg, J. P. Kerekes, O. Weatherbee, D. Messinger, J. van Aardt, E. Ientilucci *et al.*, "SpecTIR hyperspectral airborne Rochester experiment data collection campaign," in *Algorithms and Technologies for Multispectral, Hyperspectral, and Ultraspectral Imagery XVIII*, S. S. Shen and P. E. Lewis, Eds., vol. 8390, 2012.

[25] A. Plaza, Q. Du, Y.-L. Chang, and R. L. King, "High performance computing for hyperspectral remote sensing," *IEEE J. Sel. Topics Appl. Earth Observ. Remote Sens.*, vol. 4, pp. 528–544, Aug. 2011.

[26] M. J. Carlotto, "A cluster-based approach for detecting man-made objects and changes in imagery," *IEEE Trans. Geosci. Remote Sens.*, vol. 43, pp. 374–387, Feb. 2005.

[27] J. Meola, M. T. Eismann, R. L. Moses, and J. N. Ash, "Detecting changes in hyperspectral imagery using a model-based approach," *IEEE Trans. Geosci. Remote Sens.*, vol. 49, pp. 2647–2661, Jul. 2011.

[28] I. Blanes and J. Serra-Sagrista, "Pairwise orthogonal transform for spectral image coding," *IEEE Trans. Geosci. Remote Sens.*, vol. 49, pp. 961–972, Mar. 2011.

[29] S. Matteoli, N. Acito, M. Diani, and G. Corsini, "An automatic approach to adaptive local background estimation and suppression in hyperspectral target detection," *IEEE Trans. Geosci. Remote Sens.*, vol. 49, pp. 790–800, Feb. 2011.

[30] L. Capobianco, A. Garzelli, and G. Camps-Valls, "Target detection with semisupervised kernel orthogonal subspace projection," *IEEE Trans. Geosci. Remote Sens.*, vol. 47, pp. 3822–3833, Nov. 2009.

[31] S. Kraut, L. L. Scharf, and L. T. McWhorter, "Adaptive subspace detectors," *IEEE Trans. Signal Process.*, vol. 49, pp. 1–16, Jan. 2001.

[32] J. Munoz-Mari, F. Bovolo, L. Gomez-Chova, L. Bruzzone, and G. Camps-Valls, "Semisupervised one-class support vector machines for classification of remote sensing data," *IEEE Trans. Geosci. Remote Sens.*, vol. 48, pp. 3188–3197, Aug. 2010.

[33] Q. Du and I. Kopriva, "Automated target detection and discrimination using constrained kurtosis maximization," *IEEE Geosci. Remote Sens. Lett.*, vol. 5, pp. 38–42, Jan. 2008.

[34] S. Kraut and L. L. Scharf, "The CFAR adaptive subspace detector is a scale-invariant GLRT," *IEEE Trans. Signal Process.*, vol. 47, pp. 2538–2541, Sep. 1999.

[35] J. E. Fowler and Q. Du, "Anomaly detection and reconstruction from random projections," *IEEE Trans. Image Process.*, vol. 21, pp. 184–195, Jan. 2012.

[36] B. Du, L. Zhang, D. Tao, and D. Zhang, "Unsupervised transfer learning for target detection from hyperspectral images," *Neurocomputing*, vol. 120, no. 0, pp. 72–82, Nov. 23, 2013.

[37] L. Wei-Min and I. C. Chein, "Multiple-window anomaly detection for hyperspectral imagery," *IEEE J. Sel. Topics Appl. Earth Observ. Remote Sens.*, vol. 6, no. 2, pp. 644–658, Apr. 2013.

Qiandong Guo received the B.S. degree in remote sensing science and technology from Wuhan University, Wuhan, China, in 2011. He is currently working toward the M.S. degree with the Institute of Remote Sensing and Digital Earth, Chinese Academy of Sciences (CAS), Beijing, China.

His research interests include hyperspectral image processing, target detection, and artificial intelligence.

Bing Zhang (M'11–SM'12) received the B.S. degree in geography from Peking University, Beijing, China, and the M.S., and the Ph.D. degrees in remote sensing from the Institute of Remote Sensing Applications, Chinese Academy of Sciences (CAS), Beijing, China.

Currently, he is a Professor and Deputy Director of the Institute of Remote Sensing and Digital Earth, CAS. He specializes in Hyperspectral Remote Sensing and has more than 17 years of experience in studying and graduate education in this field. His study interests include development of physics-based models and image processing software for the use of hyperspectral remote sensing data in solving problems in geology, hydrology, ecology, and botany. It is remarkable that some innovative research and research-based development projects undertaken by him that have made him.

Dr. Zhang received several Chinese National, Ministerial, and Provincial S&T Progress Awards.

Qiong Ran received the B.S. degree in geography from China University of Geosciences, Wuhan, China, in 2002, and the M.S., and Ph.D. degrees in remote sensing from the Institute of Remote Sensing Applications, Chinese Academy of Sciences (CAS), Beijing, China, in 2005 and 2009, respectively.

She is currently working with the College of Information Science and Technology, Beijing University of Chemical Technology, Beijing, China. She has published over 10 papers in China and abroad. Her research interests include image acquisition, image processing, and hyperspectral image analysis and applications.

Lianru Gao (M'12) received the B.S. degree in civil engineering from Tsinghua University, Beijing, China, in 2002, and the Ph.D. degree in cartography and geographic information system from the Institute of Remote Sensing Applications, Chinese Academy of Sciences, Beijing, China, in 2007.

He is currently an Associate Professor with the Key Laboratory of Digital Earth Science, Institute of Remote Sensing and Digital Earth, Chinese Academy of Sciences. He has published over 50 papers in China and abroad. His research interests include spectral feature analysis, hyperspectral image processing, target detection, and image simulation.

Jun Li received the B.S. degree in geographic information systems from Hunan Normal University, Changsha, China, in 2004, the M.E. degree in remote sensing from Peking University, Beijing, China, in 2007, and the Ph.D. degree in electrical engineering from the Instituto de Telecomunicações, Instituto Superior Técnico (IST), Universidade Técnica de Lisboa, Lisbon, Portugal, in 2011.

From 2007 to 2011, she was a Marie Curie Research Fellow with the Departamento de Engenharia Electrotécnica e de Computadores and the Instituto de Telecomunicações, IST, Universidade Técnica de Lisboa, in the framework of the European Doctorate for Signal Processing (SIGNAL). She has also been actively involved in the Hyperspectral Imaging Network, a Marie Curie Research Training Network involving 15 partners in 12 countries and intended to foster research, training, and cooperation on hyperspectral imaging at the European level. Since 2011, she has been a Postdoctoral Researcher with the Hyperspectral Computing Laboratory, Department of Technology of Computers and Communications, Escuela Politécnica, University of Extremadura, Cáceres, Spain. Her research interests include hyperspectral image classification and segmentation, spectral unmixing, signal processing, and remote sensing.

Dr. Li has been a Reviewer of several journals, including the IEEE TRANSACTIONS ON GEOSCIENCE AND REMOTE SENSING, the IEEE GEOSCIENCE AND REMOTE SENSING LETTERS, PATTERN RECOGNITION, OPTICAL ENGINEERING, *Journal of Applied Remote Sensing*, and *Inverse Problems and Imaging*. She received the 2012 Best Reviewer Award of the IEEE JOURNAL OF SELECTED TOPICS IN APPLIED EARTH OBSERVATIONS AND REMOTE SENSING.

Antonio Plaza (M'05–SM'07) received the M.S. and the Ph.D. degrees in computer engineering from the University of Extremadura, Caceres, Spain.

He is an Associate Professor (with accreditation for Full Professor) with the Department of Technology of Computers and Communications, University of Extremadura, where he is the Head of the Hyperspectral Computing Laboratory (HyperComp). He was the Coordinator of the Hyperspectral Imaging Network, a European project with total funding of 2.8 M, in 2007–2011. He authored more than 370 publications, including more than 100 JCR journal papers (60 in IEEE journals), 20 book chapters, and over 230 peer-reviewed conference proceeding papers (90 in IEEE conferences). He has guest edited seven special issues on JCR journals (three in IEEE journals).

Dr. Plaza has been a Chair for the IEEE WORKSHOP ON HYPERSPECTRAL IMAGE AND SIGNAL PROCESSING: EVOLUTION IN REMOTE SENSING, in 2011. He is a recipient of the recognition of Best Reviewers of the IEEE GEOSCIENCE AND REMOTE SENSING LETTERS, in 2009, and a recipient of the recognition of Best Reviewers of the IEEE TRANSACTIONS ON GEOSCIENCE AND REMOTE SENSING, in 2010, a journal for which he has served as Associate Editor, in 2007–2012. He is also an Associate Editor for IEEE ACCESS and the IEEE GEOSCIENCE AND REMOTE SENSING MAGAZINE and was a member of the Editorial Board of the IEEE GEOSCIENCE AND REMOTE SENSING NEWSLETTER, in 2011–2012, and a member of the steering committee of the IEEE JOURNAL OF SELECTED TOPICS IN APPLIED EARTH OBSERVATIONS AND REMOTE SENSING, in 2012. He served as the Director of Education Activities for the IEEE GEOSCIENCE AND REMOTE SENSING SOCIETY (GRSS), in 2011–2012, and is currently serving as President of the Spanish Chapter of IEEE GRSS (since November 2012). He is currently serving as the Editor-in-Chief of the IEEE TRANSACTIONS ON GEOSCIENCE AND REMOTE SENSING JOURNAL (since January 2013). Additional information: http://www.umbc.edu/rssipl/people/aplaza.